J. Fluid Mech. (2017), vol. 822, pp. 5–30. © Cambridge University Press 2017

This is an Open Access article, distributed under the terms of the Creative Commons Attribution licence (http://creativecommons.org/licenses/by/4.0/), which permits unrestricted re-use, distribution, and reproduction in any medium, provided the original work is properly cited. doi:10.1017/ifm.2017.212

Effect of wall cooling on boundary-layer-induced pressure fluctuations at Mach 6

Chao Zhang¹, Lian Duan¹,† and Meelan M. Choudhari²

¹Missouri University of Science and Technology, Rolla, MO 65401, USA

²NASA Langley Research Center, Hampton, VA 23681, USA

(Received 23 November 2016; revised 21 February 2017; accepted 23 March 2017)

Direct numerical simulations of turbulent boundary layers with a nominal free-stream Mach number of 6 and a Reynolds number of $Re_{\tau} \approx 450$ are conducted at a wall-to-recovery temperature ratio of $T_w/T_r = 0.25$ and compared with a previous database for $T_w/T_r = 0.76$ in order to investigate pressure fluctuations and their dependence on wall temperature. The wall-temperature dependence of widely used velocity and temperature scaling laws for high-speed turbulent boundary layers is consistent with previous studies. The near-wall pressure-fluctuation intensities are dramatically modified by wall-temperature conditions. At different wall temperatures, the variation of pressure-fluctuation intensities as a function of wall-normal distance is dramatically modified in the near-wall region but remains almost intact away from the wall. Wall cooling also has a strong effect on the frequency spectrum of wall-pressure fluctuations, resulting in a higher dominant frequency and a sharper spectrum peak with a faster roll-off at both the high- and low-frequency ends. The effect of wall cooling on the free-stream noise spectrum can be largely accounted for by the associated changes in boundary-layer velocity and length scales. The pressure structures within the boundary layer and in the free stream evolve less rapidly as the wall temperature decreases, resulting in an increase in the decorrelation length of coherent pressure structures for the colder-wall case. The pressure structures propagate with similar speeds for both wall temperatures. Due to wall cooling, the generated pressure disturbances undergo less refraction before they are radiated to the free stream, resulting in a slightly steeper radiation wave front in the free stream. Acoustic sources are largely concentrated in the near-wall region; wall cooling most significantly influences the nonlinear (slow) component of the acoustic source term by enhancing dilatational fluctuations in the viscous sublayer while damping vortical fluctuations in the buffer and log layers.

Key words: high-speed flow, turbulence simulation, turbulent boundary layers

1. Introduction

An understanding of the physics of pressure fluctuations induced by high-speed turbulent boundary layers is important to the structural design of hypersonic vehicles and to the testing and evaluation of hypersonic vehicles in noisy hypersonic facilities. The fluctuating surface pressure on vehicle surfaces is responsible for vibrational load and may lead to damaging effects such as flutter. The free-stream pressure fluctuations radiated from the turbulent boundary layer on the nozzle wall of conventional hypersonic wind tunnels give rise to tunnel noise that has first-order impact on laminar–turbulent transition in the tunnel. Given that the surface temperatures of hypersonic flight vehicles are typically significantly lower than the adiabatic wall temperature and that practical hypersonic facilities for testing and evaluating hypersonic vehicles are designed to have a non-adiabatic turbulent boundary layer on the nozzle wall, it is of practical importance to investigate wall-temperature effects on hypersonic turbulent boundary layers and their induced pressure fluctuations.

To date, there is limited literature on the effects of wall cooling on high-speed turbulent boundary layers. Most of the available measurements are restricted to basic turbulence quantities, such as the skin friction and Stanton number, and the mean and root mean square (r.m.s.) fluctuations of velocity and temperature (Fernholz & Finley 1980; Smits & Dussauge 2006). Existing numerical studies are largely focused on the effect of wall cooling on the distribution and scaling of velocity fluctuations and the relationships between temperature and velocity fields at a Mach number of 5 or less (Maeder 2000; Duan, Beekman & Martín 2010; Shahab et al. 2011; Chu, Zhang & Lu 2013; Zhang et al. 2014; Hadjadj et al. 2015; Shadloo, Hadjadj & Hussain 2015; Trettel & Larsson 2016). For example, Duan et al. (2010) performed direct numerical simulations (DNS) of turbulent boundary layers at Mach 5 over a broad range of wall-to-recovery temperature ratios $(T_w/T_r = 0.18-1.0)$ and focused on assessing the validity of Morkonvin's hypothesis in the high-Mach-number cold-wall regime. Zhang et al. (2014) studied the coupling between the thermal and velocity fields of compressible wall-bounded turbulent flows and introduced a generalized Reynolds analogy that explicitly accounts for finite wall heat flux for cold-wall boundary layers. Hadjadj et al. (2015) and Shadloo et al. (2015) conducted detailed analyses of the effect of wall temperature on the statistical behaviour of turbulent boundary layers at Mach 2. Bowersox (2009) and Poggie (2015) studied the modelling of turbulent energy flux in adiabatic and cold-wall turbulent boundary layers. Trettel & Larsson (2016) introduced a new mean-velocity scaling for compressible wall turbulence with heat transfer; this new scaling achieved excellent collapse of the mean-velocity profile at different Reynolds numbers, Mach numbers and rates of wall heat transfer.

As far as the boundary-layer-induced pressure fluctuations are concerned, the body of available data is even more scarce. Experimental measurements consist largely of those at the wall using surface-mounted pressure transducers (Kistler & Chen 1963; Fernholz *et al.* 1989; Beresh *et al.* 2011). Previous DNS studies of pressure fluctuations induced by high-speed turbulent boundary layers have focused on boundary layers with adiabatic or nearly adiabatic walls (Bernardini & Pirozzoli 2011; Di Marco *et al.* 2013; Duan, Choudhari & Wu 2014; Duan, Choudhari & Zhang 2016). To the best of the knowledge of the authors, no existing studies have been conducted in the high-Mach-number cold-wall regime that provide the off-wall fluctuating pressure field including the free-stream acoustic pressure fluctuations. As a result, a comprehensive understanding of the free-stream disturbance field and its dependence on boundary-layer parameters (e.g. free-stream Mach number, wall temperature and Revnolds number) is still lacking.

$$M_{\infty}$$
 U_{∞} (m s⁻¹) ρ_{∞} (kg m⁻³) T_{∞} (K) 5.86 869.1 0.0443 55.0

TABLE 1. Free-stream conditions for Mach 6 DNS of turbulent boundary layers. The working fluid is assumed to be a perfect gas.

The objective of the current paper is to investigate the dependence of boundary-layer-induced pressure fluctuations on wall temperature for hypersonic Mach numbers. In a previous paper by the present authors (Duan *et al.* 2016), the successful application of DNS in capturing the global fluctuating pressure field has been demonstrated for a spatially developing flat-plate nominally Mach 6 turbulent boundary layer with a wall-to-recovery temperature ratio of $T_w/T_r = 0.76$. A new DNS dataset at Mach 6 with a different wall temperature ($T_w/T_r = 0.25$) from the previous Mach 6 data (Duan *et al.* 2016) is introduced for the study of wall-temperature effects. The effect of wall temperature on single- and multi-point statistics of the computed pressure fluctuations at multiple wall-normal locations (including the inner layer, the log layer, the outer layer and the free stream) is reported, including the intensity, frequency spectra, space—time correlations and propagation velocities.

The remainder of this paper is structured as follows. The flow conditions selected for numerical simulation and the numerical method used are outlined in § 2. Section 4 is focused on an analysis of statistical and structural features of pressure fluctuations at multiple wall-normal locations, highlighting their dependence on the wall temperature. The various statistics examined include pressure-fluctuation intensities, power spectral densities, two-point pressure correlations, propagation speeds and acoustic sources. Conclusions from the study are presented in § 5.

2. Simulation details

Direct numerical simulations are performed for zero-pressure-gradient cold-wall turbulent boundary layers with a free-stream Mach number of 5.86. Two DNS cases (M6Tw025 and M6Tw076) with the same free-stream conditions but different wall temperatures are examined, with the M6Tw076 case corresponding to the previous simulation by Duan et al. (2016). Table 1 outlines the free-stream conditions for the simulations, including the free-stream velocity U_{∞} , density ρ_{∞} and temperature T_{∞} . The free-stream conditions are representative of those at the nozzle exit of the Purdue Mach 6 Quiet Tunnel (BAM6QT) under noisy operation (Schneider 2001; Steen 2010). Table 2 lists the values of the mean boundary-layer parameters at the selected downstream location (x_a) for statistical analysis, including the momentum thickness θ , shape factor $H = \delta^*/\theta$ (where δ^* denotes the local displacement thickness), boundary-layer thickness δ , friction velocity $u_{\tau} = \sqrt{\tau_w/\bar{\rho}_w}$, viscous length $z_{\tau} = \mu_w/\rho_w u_{\tau}$ and different definitions of the Reynolds number, namely $Re_{\theta} \equiv \rho_{\infty}U_{\infty}\theta/\mu_{\infty}$, $Re_{\tau} \equiv \rho_w u_{\tau} \delta/\mu_w$ and $Re_{\delta 2} \equiv \rho_{\infty} U_{\infty} \theta/\mu_w$. Throughout this paper, the subscripts ∞ and w will be used to denote quantities in the free stream and at the wall respectively. The viscosity μ is calculated using Sutherland's law, $\mu = C_1 T^{3/2}/(T + C_2)$, with constants $C_1 = 1.458 \times 10^{-6}$ and $C_2 = 110.4$. The wall temperature T_w for the case M6Tw076 is similar to that at the nozzle wall of BAM6QT, corresponding to a wall-temperature ratio of $T_w/T_r \approx 0.76$, with the recovery temperature estimated as $T_r = T_{\infty}(1 + r(\gamma - 1)M_{\infty}^2/2)$ based on a recovery factor of r = 0.89. Case M6Tw025 has the same free-stream conditions and Reynolds number, Re_{τ} , as case M6Tw076 but

Case	T_w (K)	T_w/T_r	Re_{θ}	Re_{τ}	$Re_{\delta 2}$	θ (mm)	H	δ (mm) z_{τ}	$(\mu m) u_{\tau}$	$(m \ s^{-1}) \ \delta$	δ_i (mm)
M6Tw025	97.5	0.25	2121	450	1135	0.199	8.4	3.6	8.0	33.8	1.33
M6Tw076	300	0.76	9455	453	1746	0.948	13.6	23.8	52.6	45.1	13.8

TABLE 2. Boundary-layer properties at the station (x_a) selected for the analysis of the pressure field $(x_a = 88.6\delta_i)$ for case M6Tw025 and $x_a = 54.1\delta_i$ for case M6Tw076, with δ_i being the boundary-layer thickness at the domain inlet).

a lower wall temperature $(T_w/T_r \approx 0.25)$ which is more likely to be encountered in high-altitude flight. Thus, by comparing the results of cases M6Tw025 and M6Tw076, the effect of wall cooling on the pressure fluctuations can be investigated at a fixed Reynolds number Re_τ .

Wall cooling causes a change in both the boundary-layer thickness and the fluid properties across the boundary layer. Experiments and numerical data suggest that a single Reynolds number is not sufficient to characterize the flow (Smits 1991; Lele 1994). However, what definition of the Reynolds number is 'correct' for assessing the effects of wall cooling is still an open question, and the choice of that definition mainly depends on researcher preference and the research objective (Shadloo et al. 2015). For instance, out of the few existing DNS studies on the effect of wall temperature, Maeder (2000), Lagha et al. (2011) and Shadloo et al. (2015) have chosen to match Re_{τ} for reporting their data; Duan et al. (2010) and Chu et al. (2013) have chosen to match $Re_{\delta 2}$; Shahab et al. (2011) have chosen to match Re_{θ} . In addition, Shadloo et al. (2015) compared the effects of choosing different definitions of the Reynolds number $(Re_{\tau}, Re_{\delta 2}, Re_{\theta})$ on the turbulence statistics and showed that Re_{τ} performs best in collapsing the first- and second-order statistical moments for boundary layers with different wall heat transfer values. In the current study, we have chosen to match Re_{τ} based partially on the findings of Shadloo et al. (2015). This selection of the Reynolds number is also due to our decisions with regard to grid resolutions and the limited extent of the computational domain.

The details of the DNS methodology, including numerical methods and initial and boundary conditions, have been documented in our previous papers (Duan et al. 2014, 2016). The DNS methodology has been extensively validated against experiments and existing numerical simulations for capturing boundary-layer-induced pressure fluctuations at supersonic/hypersonic speeds (Duan et al. 2014, 2016). In particular, the computational predictions for the mean-velocity profiles and surface pressure spectrum are in good agreement with experimental measurements for case M6Tw076 (Duan et al. 2016).

Figure 1 shows the computational set-up for case M6Tw025, which parallels that of case M6Tw076 documented in Duan *et al.* (2016). The computational domain size and grid resolution are determined based on the lessons learnt from Duan *et al.* (2014, 2016), as summarized in table 3. The streamwise length L_x is adjusted to ensure that the turbulence fluctuations are uncorrelated and minimal spurious correlation can be introduced due to the inflow turbulence generation. The streamwise domain size is also large enough so that the free-stream acoustic field has gone through the transient adjustment due to recycled inflow and has re-established equilibrium at the downstream location selected for statistical analysis ($x_a = 88.6\delta_i$). It can be shown that the pressure fluctuations both at the wall and in the free stream for case M6Tw025 have become homogeneous in the streamwise direction

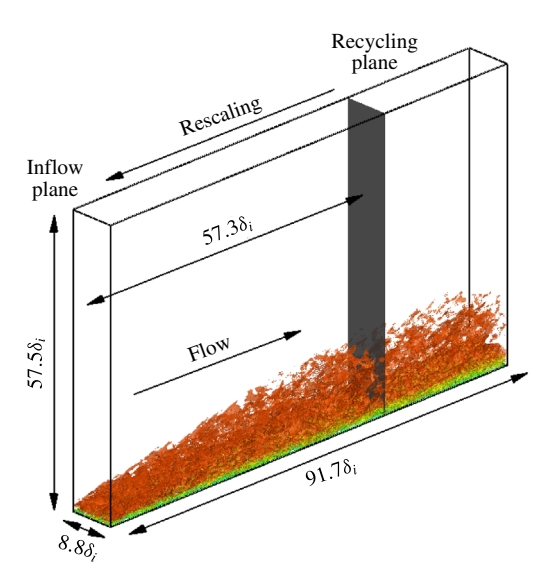


FIGURE 1. (Colour online) Computational domain and simulation set-up for the DNS case M6Tw025. The reference length δ_i is the thickness of the boundary layer (based on 99% of the free-stream velocity) at the inlet plane. An instantaneous flow is shown in the domain, visualized by the isosurface of the magnitude of the density gradient, $|\nabla \rho|\delta_i/\rho_\infty=0.98$, coloured by the streamwise velocity component (with levels from 0 to U_∞ , blue to red). Here, x, y and z are the streamwise, spanwise and wall-normal coordinates respectively.

$$N_x \times N_y \times N_z$$
 L_x/δ_i L_y/δ_i L_z/δ_i Δx^+ Δy^+ Δz_{min}^+ Δz_{max}^+ 2400 × 400 × 560 91.7 8.8 57.5 6.42 3.72 0.46 4.75

TABLE 3. Grid resolution and domain size for case M6Tw025. Here, L_x , L_y and L_z represent the domain size in the streamwise, spanwise and wall-normal directions respectively. The viscous length scale $z_\tau = 8.0~\mu m$ corresponds to $x_a/\delta_i = 88.6$. The terms Δz_{min}^+ and Δz_{max}^+ are the minimum and maximum wall-normal grid spacings for $0 \le z/\delta_i \le 8$; $\delta_i = 1.33~mm$.

after $x/\delta_i \approx 60$. Uniform grid spacings are used in the streamwise and spanwise directions. The grids in the wall-normal direction are clustered in the boundary layer with $\Delta z^+ = 0.46$ at the wall, and are kept uniform with $\Delta z^+ \approx 5$ in the free stream until up to approximately $8\delta_i$ or 3.3δ , where δ_i and δ represent the mean boundary-layer thickness based on $\overline{u}/U_\infty = 0.99$ at the inflow boundary and at the selected downstream location x_a respectively. For the selected grid resolution, the wavelength of the highest-frequency spectral components of free-stream pressure fluctuations (corresponding to $\omega \delta^*/U_\infty \approx 15$, as shown in § 4.2) is discretized with at least nine points in the streamwise direction and 12 points in the wall-normal direction.

In the following sections, averages are first calculated over a streamwise window $([x_a - 0.5\delta_i, x_a + 0.5\delta_i]$, with $x_a = 88.6\delta_i$, for case M6Tw025 and $[x_a - 0.9\delta_i, x_a + 0.9\delta_i]$, with $x_a = 54.1\delta_i$, for case M6Tw076) and the spanwise direction for each instantaneous flow field; then, an ensemble average over 312 flow-field snapshots (corresponding

to $\delta_i/U_\infty \approx 1016$ or $\delta/u_\tau \approx 14.6$) and over 153 flow-field snapshots (corresponding to $\delta_i/U_\infty \approx 240$ or $\delta/u_\tau \approx 7.2$) is calculated for cases M6Tw025 and M6Tw076 respectively. A smaller number of flow-field snapshots was sufficient for case M6Tw076 because of the larger spanwise domain size $(L_v/\delta_i = 15.7)$ for this case compared with that for case M6Tw025 ($L_v/\delta_i = 8.8$). The effect of spanwise domain size on flow statistics is monitored by comparing case M6Tw076 with an auxiliary simulation of the same grid resolution but with a narrower span of $L_{\nu}/\delta_i = 6.26$, and negligible difference is observed in the flow statistics of interest. The outflow boundary condition has no influence on boundary-layer profiles within the selected streamwise window over which averages are calculated. Statistical convergence for both cases is verified by calculating averages over varying streamwise window sizes or over a different number of snapshots and by making sure that the differences in flow statistics are negligible (<1%) among the different data-averaging techniques. Data for free-stream acoustic radiation were not sampled at the same value of z/δ for the two cases. Therefore, comparison of statistical and spectral characteristics will be made between predictions at $z/\delta = 2.36$ (i.e. $z_{\infty} = 2.36\delta$) for case M6Tw025 and $z/\delta = 2.63$ (i.e. $z_{\infty} = 2.63\delta$) for case M6Tw076. Throughout the paper, standard (Reynolds) averages are denoted by an overbar, \bar{f} , and fluctuations around standard averages are denoted by a single prime, as $f' = f - \bar{f}$. Negligible differences have been found between the standard and density-weighted (Favre) averages for the statistics reported in this article.

3. Assessment of DNS data

In this section, the first- and second-moment statistics of the velocity and temperature fields are reported at the selected downstream location (x_a) . The data are compared with published data, especially those of turbulent boundary layers in the hypersonic cold-wall regime.

Figure 2(a) plots the van Driest transformed mean velocity u_{VD}^+ , which is defined as

$$u_{VD}^{+} = \frac{1}{u_{\tau}} \int_{0}^{\overline{u}} (\overline{\rho}/\overline{\rho}_{w})^{1/2} d\overline{u}.$$
 (3.1)

The mean velocity shows an approximately logarithmic region where $u_{VD}^+ = (1/k) \log(z^+) + C$ upon van Driest transformation. Consistent with the published data by Duan *et al.* (2010), Shadloo *et al.* (2015), Modesti & Pirozzoli (2016) and Wu *et al.* (2017), the van Driest-transformed mean velocity shows a shrinking of the linear viscous sublayer with higher wall cooling, while the additive constant C in the log law does not seem to be significantly affected. Figure 2(b) shows a significantly better collapse of data in both the viscous sublayer and the log layer among the computational datasets involving different wall-cooling rates, after the mean velocity and the wall-normal coordinate are transformed according to the proposal by Trettel & Larsson (2016) as

$$u_{TL}^{+} = \int_{0}^{u^{+}} \left(\frac{\bar{\rho}}{\rho_{w}}\right)^{1/2} \left[1 + \frac{1}{2} \frac{1}{\bar{\rho}} \frac{d\bar{\rho}}{dz} z - \frac{1}{\bar{\mu}} \frac{d\bar{\mu}}{dz} z\right] du^{+}, \quad z^{*} = \frac{\bar{\rho} (\tau_{w}/\bar{\rho})^{1/2} z}{\bar{\mu}}.$$
 (3.2*a,b*)

Figure 3 plots the streamwise turbulence intensity and the Reynolds shear stress. A significantly improved collapse of data is achieved by Morkovin's scaling (Morkovin 1962), which takes into account the variation in mean flow properties.

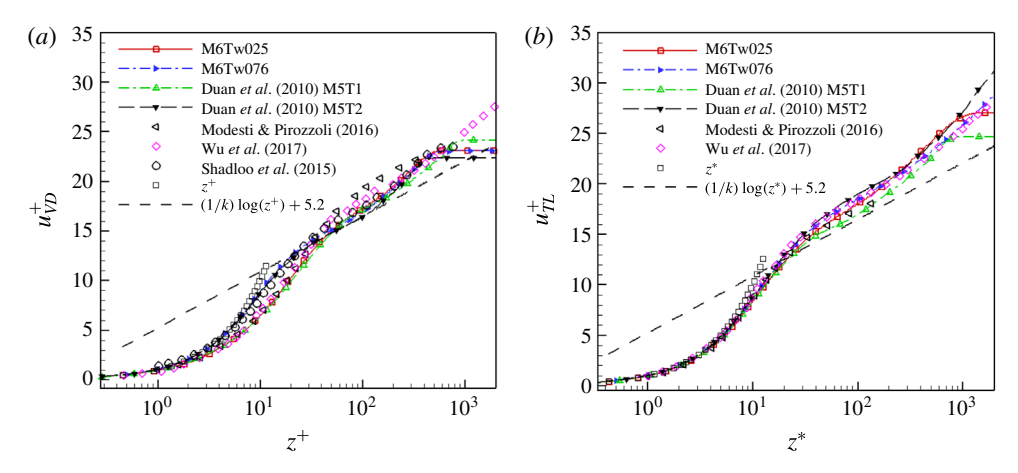


FIGURE 2. (Colour online) Mean-velocity profiles transformed according to (*a*) van Driest and (*b*) Trettel & Larsson (2016). Symbols: △ (green), Duan *et al.* (2010) M5T1, $M_{\infty} = 5$, $Re_{\tau} = 798$, $T_w/T_r = 0.18$; ▼, Duan *et al.* (2010) M5T2, $M_{\infty} = 5$, $Re_{\tau} = 386$, $T_w/T_r = 1.0$; ⊲, Modesti & Pirozzoli (2016), $M_{\infty} = 1.9$, $Re_{\tau} = 448$, $T_w/T_r = 0.24$; \diamondsuit (violet red), Wu *et al.* (2017), $M_{\infty} = 4.5$, $Re_{\tau} = 2200$, $T_w/T_r = 0.22$; \diamondsuit , Shadloo *et al.* (2015), $M_{\infty} = 2$, $Re_{\tau} = 507$, $T_w/T_r = 0.5$.

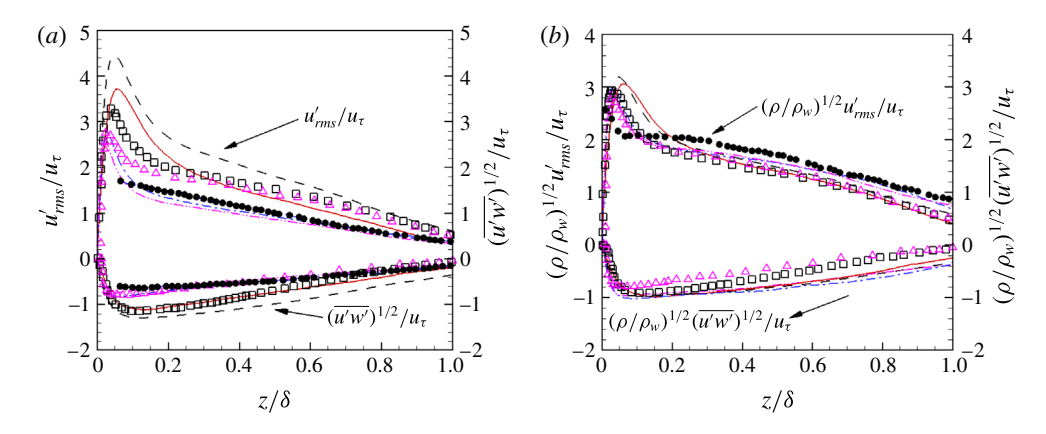


FIGURE 3. (Colour online) Distribution of r.m.s. velocity components as a function of wall-normal distance. Curves and symbols: —— (red), M6Tw025, $M_{\infty} = 5.86$, $Re_{\tau} = 450$, $T_w/T_r = 0.25$; ---- (blue), M6Tw076, $M_{\infty} = 5.86$, $Re_{\tau} = 453$, $T_w/T_r = 0.76$; ---, Duan et al. (2010), $M_{\infty} = 5$, $Re_{\tau} = 798$, $T_w/T_r = 0.18$; —---, Duan et al. (2010), $M_{\infty} = 5$, $Re_{\tau} = 386$, $T_w/T_r = 1.0$; \Box Shadloo et al. (2015), $M_{\infty} = 2$, $Re_{\tau} = 507$, $T_w/T_r = 0.5$; Δ (violet red), Schlatter & Örlü (2010), $M_{\infty} \approx 0$, $Re_{\tau} = 500$; \Box , Peltier, Humble & Bowersox (2016), $M_{\infty} = 4.9$, $Re_{\tau} = 1100$, $T_w/T_r = 0.9$.

Morkovin's scaling brings the magnitudes of the extrema in the compressible cases closer to the incompressible results of Schlatter & Örlü (2010). The better collapse of data between cases M6Tw025 and M6Tw076 in figure 3(b) indicates that the effect of wall cooling on fluctuating velocity intensities can be largely accounted for by Morkovin's scaling. Similarly improved collapse of data is achieved by Morkovin's scaling for turbulence intensities in the spanwise and wall-normal directions.

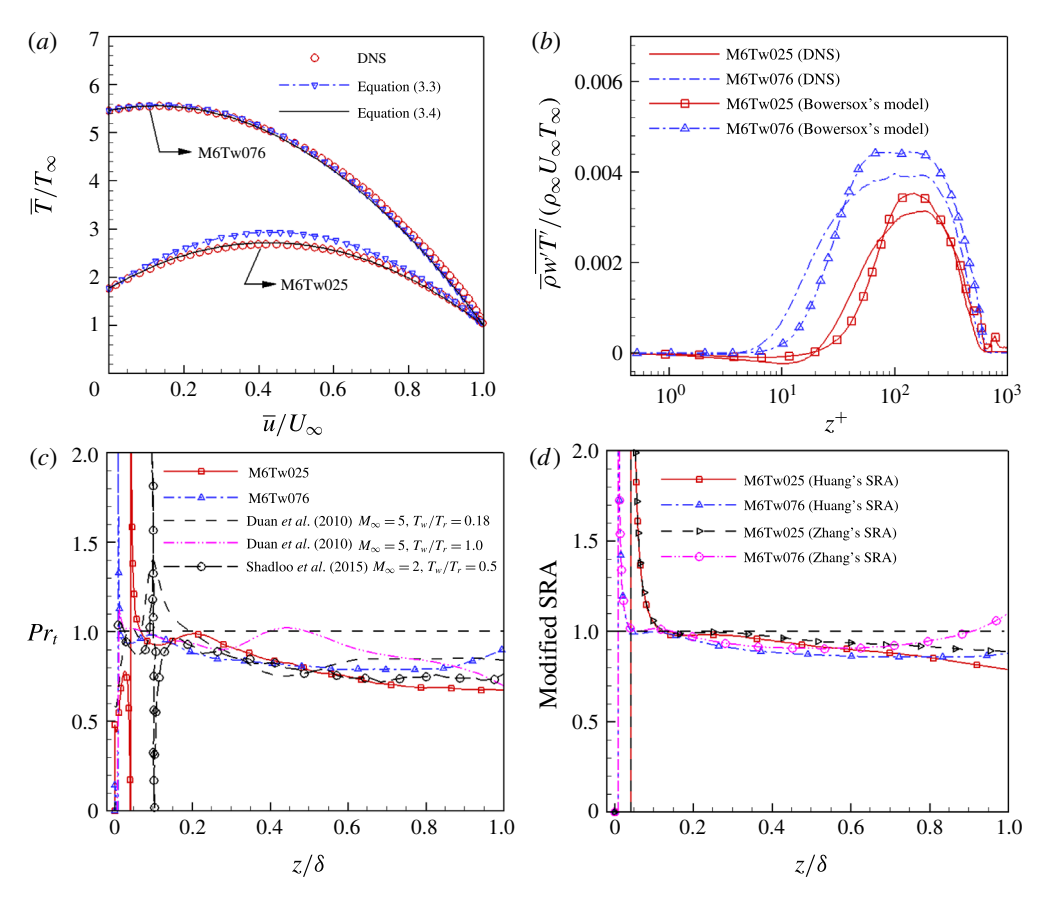


FIGURE 4. (Colour online) The coupling between thermal and velocity fields: (a) mean temperature–velocity relation; (b) DNS-predicted turbulent heat flux and the theoretical model of Bowersox (2009); (c) turbulent Prandtl number Pr_t ; (d) modified SRAs of Huang, Coleman & Bradshaw (1995) and Zhang et al. (2014). Curves and symbols: ---, Duan et al. (2010), $M_{\infty} = 5$, $Re_{\tau} = 798$, $T_w/T_r = 0.18$; —·--, Duan et al. (2010), $M_{\infty} = 5$, $Re_{\tau} = 386$, $T_w/T_r = 1.0$; O, Shadloo et al. (2015), $M_{\infty} = 2$, $Re_{\tau} = 507$, $T_w/T_r = 0.5$.

As far as the coupling between thermal and velocity fields is concerned, figure 4 plots several temperature–velocity scalings for high-speed turbulent boundary layers, including the mean temperature–velocity relation, the turbulent heat flux $\overline{\rho}w'T'$, the turbulent Prandtl number $Pr_t \equiv (\overline{\rho}u'w'(\partial \overline{T}/\partial z))/(\overline{\rho}w'T'(\partial \overline{u}/\partial z))$ and the modified strong Reynolds analogies (SRAs) of Huang *et al.* (1995) and Zhang *et al.* (2014). The present spatial DNS results at Mach 6 are generally consistent with the predictions from several previous studies at lower Mach numbers (Duan *et al.* 2010; Zhang *et al.* 2014; Shadloo *et al.* 2015) with regard to the wall-temperature dependence of the temperature–velocity scalings. In particular, figure 4(*a*) shows that strong wall cooling causes a deviation of the DNS from Walz's relation (Walz 1969), which is commonly used to relate the mean temperature and velocity as

$$\frac{\bar{T}}{T_{\infty}} = \frac{T_w}{T_{\infty}} + \frac{T_r - T_w}{T_{\infty}} \left(\frac{\bar{u}}{U_{\infty}}\right) + \frac{T_{\infty} - T_r}{T_{\infty}} \left(\frac{\bar{u}}{U_{\infty}}\right)^2. \tag{3.3}$$

A significantly improved comparison for the cold-wall case (case M6Tw025) is achieved by using the generalized Reynolds analogy of Zhang *et al.* (2014), in which a general recovery factor r_g is introduced and T_r in equation (3.3) is accordingly replaced by T_{rg} as

$$\frac{\bar{T}}{T_{\infty}} = \frac{T_w}{T_{\infty}} + \frac{T_{rg} - T_w}{T_{\infty}} \left(\frac{\bar{u}}{U_{\infty}}\right) + \frac{T_{\infty} - T_{rg}}{T_{\infty}} \left(\frac{\bar{u}}{U_{\infty}}\right)^2,\tag{3.4}$$

where $T_{rg} = T_{\infty} + r_g U_{\infty}^2/(2C_p)$ with $r_g = 2C_p (T_w - T_{\infty})/U_{\infty}^2 - 2Prq_w/(U_{\infty}\tau_w)$, where Pr is the molecular Prandtl number and C_p is the heat capacity at constant pressure. Equation (3.4) explicitly accounts for the wall heat flux q_w , and it coincides with Walz's relation in the case of adiabatic walls.

Figure 4(b) shows that the DNS-predicted turbulent heat flux $\overline{\rho}\overline{w'T'}$ compares well with the prediction of the theoretical model by Bowersox (2009), consistent with the finding by Poggie (2015). The DNS-predicted turbulent Prandtl number compares well with the computations of Shadloo *et al.* (2015) and shows singular behaviour near the wall where the correlation $\overline{w'T'}$ is zero (figure 4c). The SRA relates the temperature fluctuations T'_{rms} to the streamwise velocity fluctuations u'_{rms} , as given by

$$\frac{T'_{rms}/\overline{T}}{(\gamma - 1)M^2(u'_{rms}/\overline{u})} = \frac{1}{a(1 - (\partial \overline{T}_t/\partial \overline{T}))},$$
(3.5)

where $a = Pr_t$ in Huang's modified SRA (Huang *et al.* 1995) and $a = \overline{Pr_t} \equiv Pr_t(1 + \overline{w}\rho'u'/\overline{\rho u'w'})/(1 + \overline{w}\rho'T'/\overline{\rho w'T'})$ in Zhang's version of the modified SRA (Zhang *et al.* 2014), and $M = \overline{u}/\sqrt{\gamma RT}$ is the local Mach number. Figure 4(*d*) shows that the modified SRA of Zhang *et al.* (2014) gives a slightly improved prediction between u'_{rms} and T'_{rms} than that of Huang *et al.* (1995).

4. Boundary-layer-induced pressure fluctuations

In this section, the statistical and spectral characteristics of pressure fluctuations induced by hypersonic cold-wall turbulent boundary layers are discussed, highlighting their dependence on the wall temperature. The pressure statistics analysed include the fluctuation intensity, frequency power spectral density, space—time correlations and propagation speed.

The frequency spectrum of the pressure fluctuations is defined as

$$\Phi_p(\omega, x, z) = \frac{1}{2\pi} \int_{-\infty}^{\infty} \overline{p'(x, y, z, t)p'(x, y, z, t + \tau)} e^{-i\omega\tau} d\tau, \qquad (4.1)$$

where the overbar indicates an average over the local streamwise window, the spanwise (y) direction and the time (t). Power spectra for case M6Tw025 are calculated using the Welch method (Welch 1967) with 12 segments and 50% overlap. A Hanning window is used for weighting the data prior to the fast Fourier transform processing. The sampling frequency is approximately 31 U_{∞}/δ_i (corresponding to 20 MHz), and the length of an individual segment is approximately 156 δ_i/U_{∞} for case M6Tw025. The calculation of power spectra for case M6Tw076 follows that described in Duan *et al.* (2016). For both cases, the power spectra do not change upon changing the window function between Hanning and Hamming windows (at

least in the reported frequency ranges), and negligible differences are found when the number of data segments is varied from eight to 12.

The two-point space-time correlation coefficient of the pressure field is defined as

$$C_{pp}(\Delta x, \Delta y, \Delta t, x, z, z_{ref}) = \frac{\overline{p'(x, y, z_{ref}, t)p'(x + \Delta x, y + \Delta y, z, t + \Delta t)}}{\left(\overline{p'^2(x, y, z_{ref}, t)}\right)^{1/2} \left(\overline{p'^2(x + \Delta x, y + \Delta y, z, t + \Delta t)}\right)^{1/2}},$$
(4.2)

where Δx and Δy are the spatial separations in the streamwise and spanwise directions respectively, Δt is the time delay and z_{ref} is the wall-normal location at which the correlation is computed.

4.1. Root mean square of pressure fluctuations

In this section, the wall-normal variation of pressure statistics for the cold-wall hypersonic turbulent boundary layer (case M6Tw025) is discussed. The results are compared with turbulent boundary layers with an adiabatic or nearly adiabatic wall to highlight the effect of wall cooling.

Figures 5(a) and 5(b) show the profiles of the r.m.s. of pressure fluctuations p'_{rms} normalized by the local wall shear stress τ_w . For case M6Tw025, p'_{rms}/τ_w undergoes a rapid increase in magnitude as $z \to 0$, with $p'_{rms}/\tau_w \approx 3.5$ at the wall and $p'_{rms}/\tau_w \approx 2.2$ at $z/\delta \approx 0.08$. The magnitude of pressure fluctuation nearly plateaus for $0.08 \lesssim z/\delta \lesssim 0.2$. For case M6Tw076 and the DNS results of Bernardini & Pirozzoli (2011), however, a similarly rapid increase in the magnitude of pressure fluctuation with respect to τ_w as $z \to 0$ is not observed. Instead, the maximum of p'_{rms}/τ_w is located away from the wall at $z/\delta \approx 0.08$ ($z^+ \approx 25$). The peak of p'_{rms}/τ_w is approximately 20% lower in magnitude for case M6Tw076 than for case M6Tw025. The large difference in p'_{rms}/τ_w values close to the wall between the turbulent boundary layer with a cold wall (case M6Tw025) and those with an adiabatic or nearly adiabatic wall (case M6Tw076 and that by Bernardini & Pirozzoli (2011)) indicates a strong influence of wall cooling on the pressure fluctuations near the wall. The influence of wall cooling on p'_{rms}/τ_w becomes much weaker in the outer part of the boundary layer $(z/\delta > 0.3)$ and nearly vanishes in the free stream. Outside the boundary layer, p'_{rms}/τ_w approaches a constant value of $p'_{rms}/\tau_w \approx 0.9$ for both the M6Tw025 and M6Tw076 cases. Figures 5(a) and 5(b) show the profiles of r.m.s. pressure fluctuations normalized by the local wall shear stress p'_{rms}/τ_w . Figures 5(c) and 5(d) further plot the profiles of r.m.s. pressure fluctuations p'_{rms} normalized by the local mean (static) pressure \bar{p} and the free-stream dynamic pressure $q_{\infty}=0.5\rho_{\infty}U_{\infty}^2$ respectively. In contrast to the similar values of p'_{rms}/τ_w , significantly different values of p'_{rms}/\overline{p} and p'_{rms}/q_{∞} are shown throughout the boundary layer between cases M6Tw025 and M6Tw076, indicating that the mean shear stress τ_w is a better scaling for p'_{rms} than the mean and dynamic pressures that account for the effect of wall cooling.

4.2. Frequency spectra of pressure fluctuations

Figure 6 compares the wall-pressure spectra of cases M6Tw025 and M6Tw076. The spectra are normalized so that the area under each curve is equal to unity. For reference, straight lines with slopes of 2, -1, -7/3 and -5 are also included to gauge the rate of spectral roll-off across relatively low, mid, mid-to-high overlap and

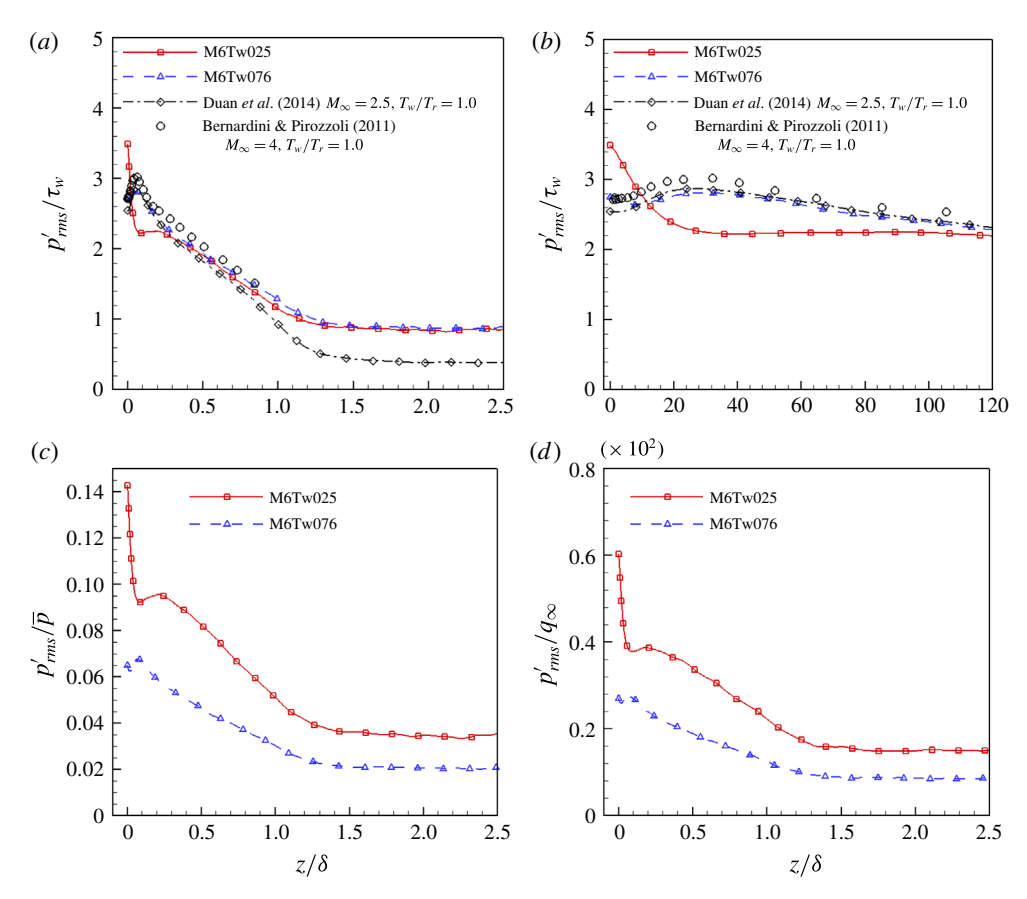


FIGURE 5. (Colour online) Pressure-fluctuation r.m.s. profile p'_{rms} as a function of wall-normal distance normalized by (a,b) the local wall shear stress τ_w , (c) the mean pressure \bar{p} and (d) the dynamic pressure q_{∞} . Symbols: \diamondsuit , Duan *et al.* (2014), $M_{\infty} = 2.5$, $Re_{\tau} = 510$, $T_w/T_r = 1.0$; \bigcirc , Bernardini & Pirozzoli (2011), $M_{\infty} = 4$, $Re_{\tau} = 506$, $T_w/T_r = 1.0$.

high frequencies respectively, according to Bull (1996). The wall-pressure spectrum shows a strong wall-temperature dependence, especially in regions of mid frequencies (i.e. $\omega \delta^*/U_{\infty} > 0.03$ and $\omega v/u_{\tau}^2 < 0.3$) and mid-to-high overlap frequencies (i.e. $0.3 < \omega v/u_{\tau}^2 < 1$), and neither the outer scaling (figure 6a) nor the inner scaling (figure 6b) collapses the spectrum between the two DNS cases. Given that the pressure spectrum at mid frequencies is typically attributed to convected turbulence in the logarithmic region and that at mid-to-high overlap frequencies is attributed to eddies in the highest part of the buffer region $(20 < z^+ < 30)$ (Bull 1996), the large variation in the wall-pressure spectrum at mid and mid-to-high overlap frequencies with wall cooling is consistent with the large changes in eddies in buffer and log layers, as reflected by the differences in r.m.s. pressure values in figure 5. The deviation from Kolmogorov's -7/3 scaling in the overlap region between mid and high frequencies is consistent with the findings of Tsuji et al. (2007) and Bernardini, Pirozzoli & Grasso (2011). At both wall temperatures, the wall-pressure spectrum shows a rather weak frequency dependence at the lowest computed frequencies and exhibits the ω^{-5} scaling predicted theoretically by Blake (1986) at the highest computed frequencies. The premultiplied wall-pressure spectrum for case M6Tw025

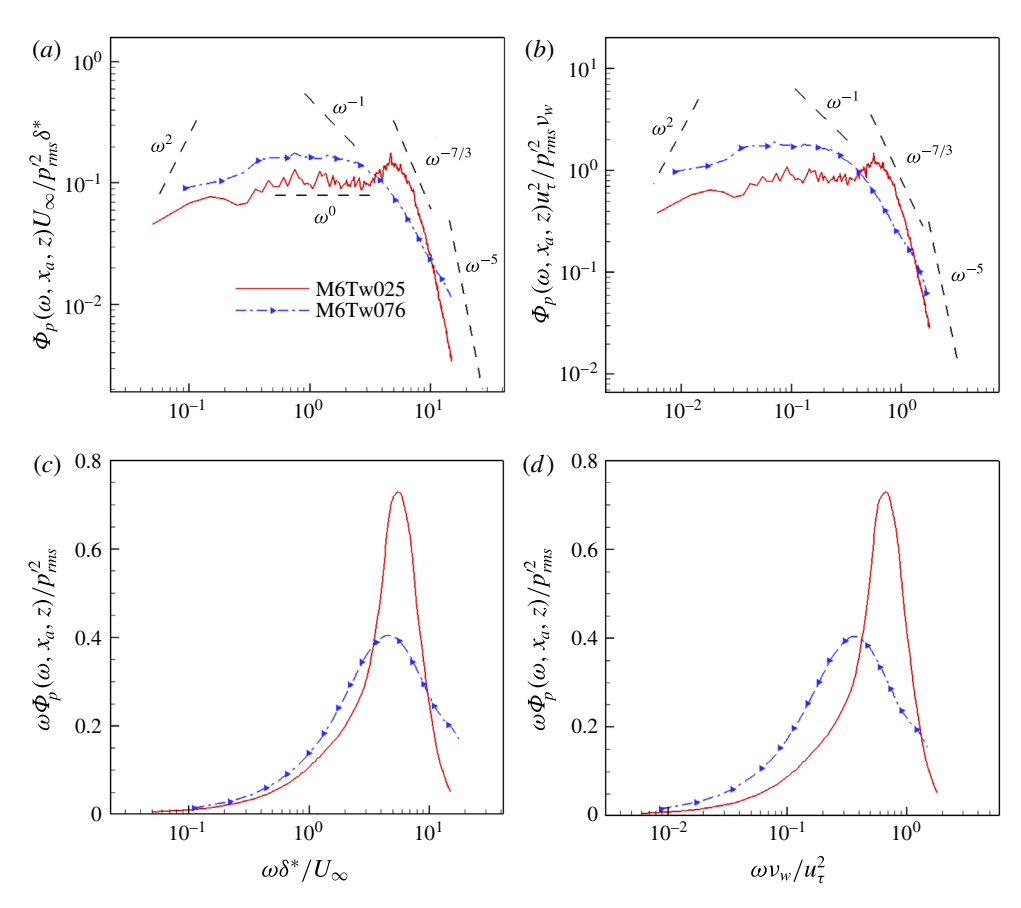


FIGURE 6. (Colour online) Comparison of pressure spectra at the wall (z=0) between cases M6Tw025 and M6Tw076. The pressure spectrum is normalized so that the area under each curve is equal to unity. (a) Log-log plot in outer scale; (b) log-log plot in inner scale; (c) log-linear plot in outer scale; (d) log-linear plot in inner scale. The area under each curve is equal to unity. The value of p'_{rms} at the wall is 100.8 Pa for case M6Tw025 and 44.3 Pa for case M6Tw076.

(figure 6c,d) consists of a sharper peak with a faster roll-off at both high and low frequencies compared with case M6Tw076, and wall cooling causes an increase in the dominant frequency from $\omega \delta^*/U_\infty \approx 4$ ($\omega v_w/u_\tau^2 = 0.4$ or $f\delta/U_\infty = 1.2$) for case M6Tw076 to $\omega \delta^*/U_\infty \approx 5$ ($\omega v_w/u_\tau^2 = 0.6$ or $f\delta/U_\infty = 1.7$) for case M6Tw025.

Regarding the free-stream pressure spectra, figure 7(a) shows that the low-frequency range of the pressure spectra Φ_p is relatively insensitive to T_w/T_r when expressed in outer variables, and figure 7(b) shows that the high-frequency portions nearly overlap in inner variables, which conforms to the findings of the wall-pressure spectrum in low-speed adiabatic flows (Bull 1996). Moreover, figures 7(c) and 7(d) show that the peak of the premultiplied spectrum is centred at a frequency of $\omega \delta^*/U_\infty \approx 1.5$, which is more than three times lower than that of the pressure spectrum at the wall, indicating that the characteristic frequency of the acoustic mode is significantly lower than that of the vortical fluctuation close to the surface. The dominant frequency of the free-stream pressure spectrum is independent of wall temperature, indicating relatively insignificant influence of wall cooling on the free-stream pressure spectrum.

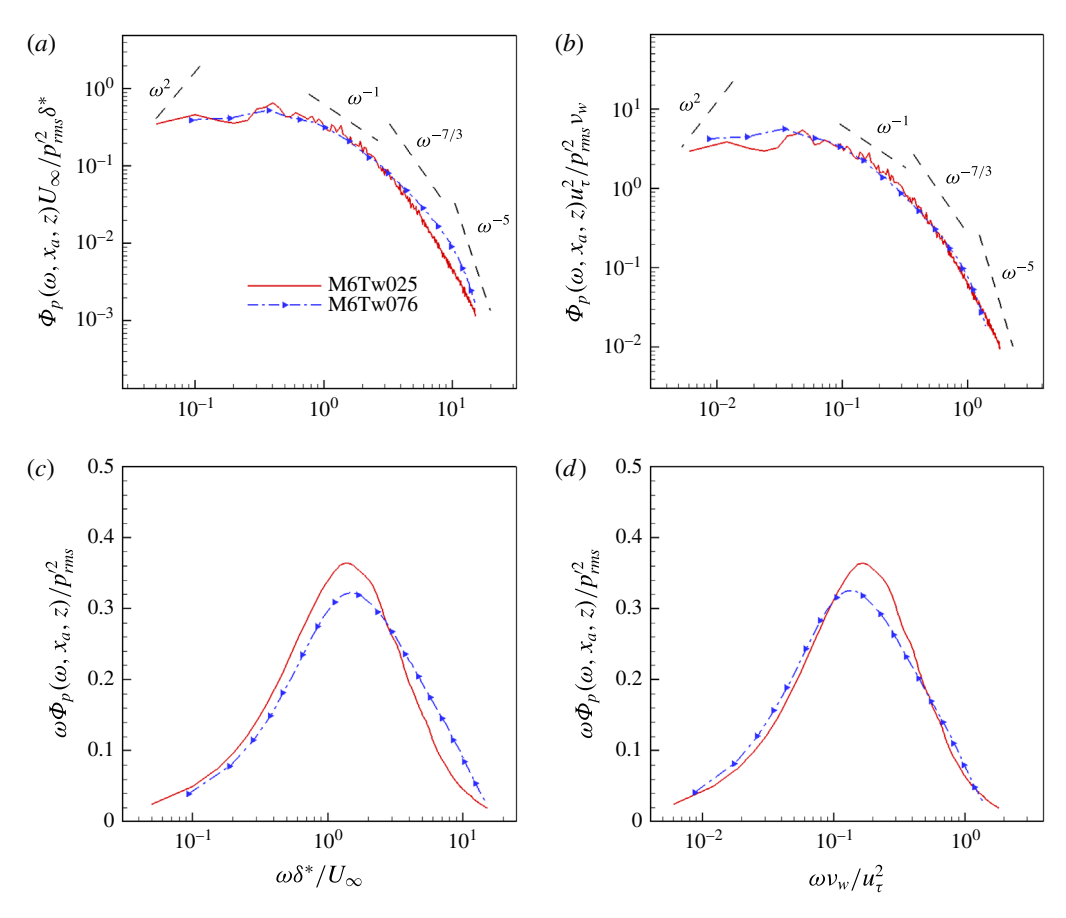
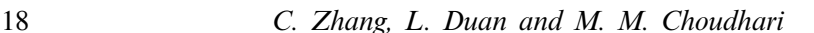


FIGURE 7. (Colour online) Comparison of pressure spectra in the free stream ($z=z_{\infty}$) between cases M6Tw025 and M6Tw076: (a) log-log plot in outer scale; (b) log-log plot in inner scale; (c) log-linear plot in outer scale; (d) log-linear plot in inner scale. The area under each curve is equal to unity. The value of p'_{rms} in the free stream is 24.8 Pa for case M6Tw025 and 13.9 Pa for case M6Tw076.

4.3. Spatial correlation of pressure fluctuations

To illustrate the spatial size and orientation of statistically significant three-dimensional (3D) pressure structures, figure 8 plots the 3D correlation coefficient of the pressure signal $C_{pp}(\Delta x, \Delta y, 0, x_a, z, z_{ref})$ as a function of wall-normal distance. For each reference height z_{ref} , there exists a downward-leaning pressure structure with finite spatial size and an inclined orientation. The pressure structure has a spatial length scale of the order of the boundary-layer thickness $O(\delta)$ in each direction and increases in size as the distance from the wall increases. The pressure structure is approximately perpendicular to the direction of U_{∞} at the wall and becomes increasingly more downward leaning as it moves away from the wall in the inner and outer regions of the boundary layer. In the free stream, the inclination angle with respect to the direction of U_{∞} approaches $\theta_{xz} \approx 28^{\circ}$. The free-stream wave-front orientation closely matches the wave-front orientation of the instantaneous acoustic radiation visualized by numerical schlieren image, as will be shown in figure 9. Consistent with the spatial correlation in the free-stream region (figure 8d), the 3D visualization



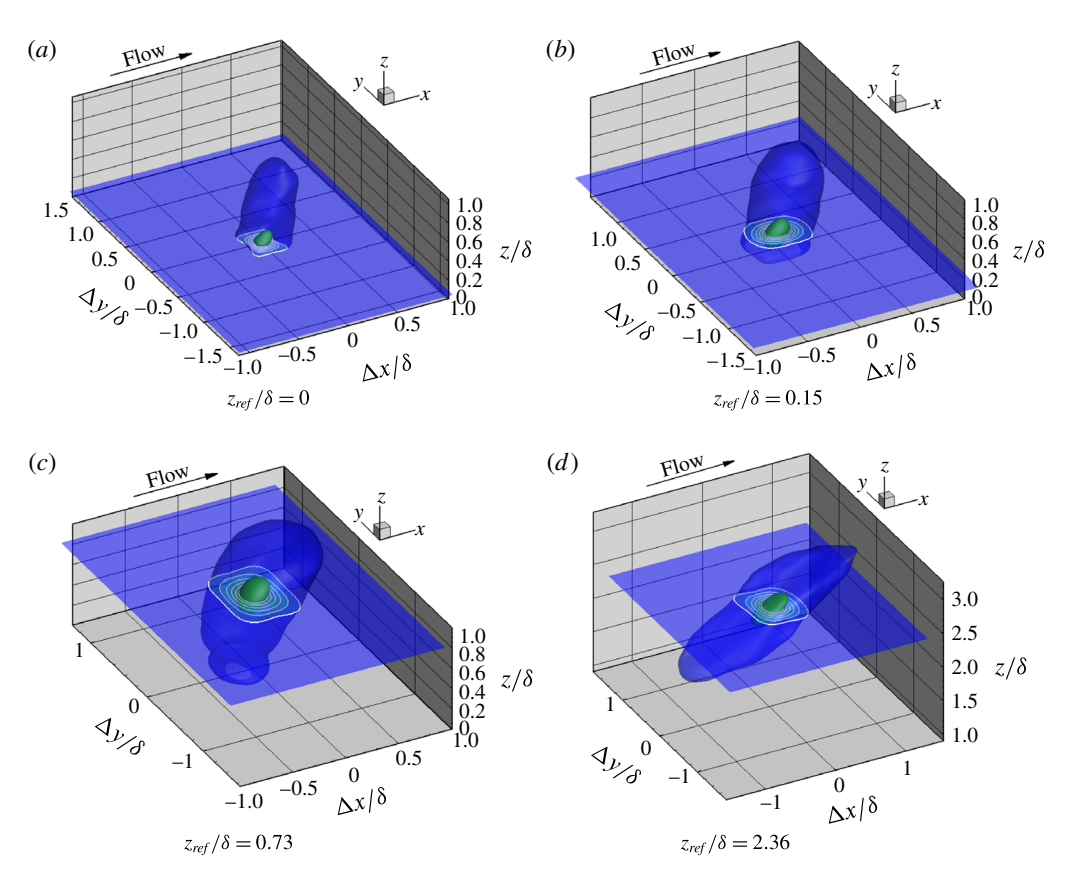


FIGURE 8. (Colour online) Three-dimensional representation of the spatial correlation coefficient $C_{pp}(\Delta x, \Delta y, 0, x_a, z, z_{ref})$ of the pressure signal at multiple wall-normal locations for case M6Tw025. The flow goes from left to right towards the positive x direction. Three-dimensional isosurfaces are shown at $C_{pp} = 0.1$ (blue) and 0.6 (green). In the horizontal planes going through the correlation origin $(z = z_{ref})$, the contour lines shown in white range from 0.1 to 0.9.

in figure 9 shows that the free-stream pressure waves deviate from purely planar behaviour in the spanwise wall-normal (y-z) plane and exhibit a preferred orientation of $\theta \approx 28^{\circ}$ in the streamwise wall-normal (x-z) plane. The finite spanwise extent of the free-stream pressure waves is consistent with the finite size of acoustic sources that are responsible for generating the waves. Similar patterns of free-stream acoustic radiation are also found for case M6Tw076 (Duan *et al.* 2016).

Figure 10 compares the spatial correlation coefficient (with zero spanwise separation, $\Delta y = 0$) in the streamwise wall-normal plane between cases M6Tw025 and M6Tw076. At the wall ($z_{ref}/\delta = 0$), the pressure structures have a similar inclination angle of $\theta_{xz} \approx 81^{\circ}$ for both cases. In the free stream, the structure angle for cases M6Tw025 and M6Tw076 decreases to $\theta_{xz} \approx 28^{\circ}$ and $\theta_{xz} \approx 21^{\circ}$ respectively. The change in inclination might indicate that pressure disturbances generated within the boundary layer undergo less refraction before they are radiated to the free stream, resulting in a higher wave angle for case M6Tw025. The reduction in refraction for case M6Tw025 may be due to the less drastic variation in fluid properties (such as fluid density and temperature) because of wall cooling.

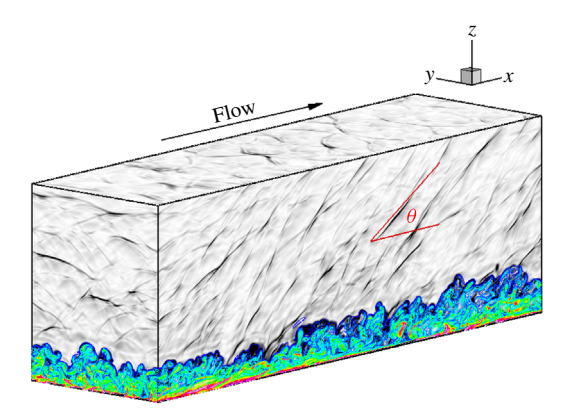


FIGURE 9. (Colour online) Instantaneous flow visualization for case M6Tw025. The grey contours are those of numerical schlieren, with density gradient contour levels selected to emphasize disturbances in the free stream. The colour contours are those of the magnitude of vorticity, with contour levels selected to emphasize the large-scale motions within the boundary layer. The angle θ is between the flow direction and the acoustic wave front.

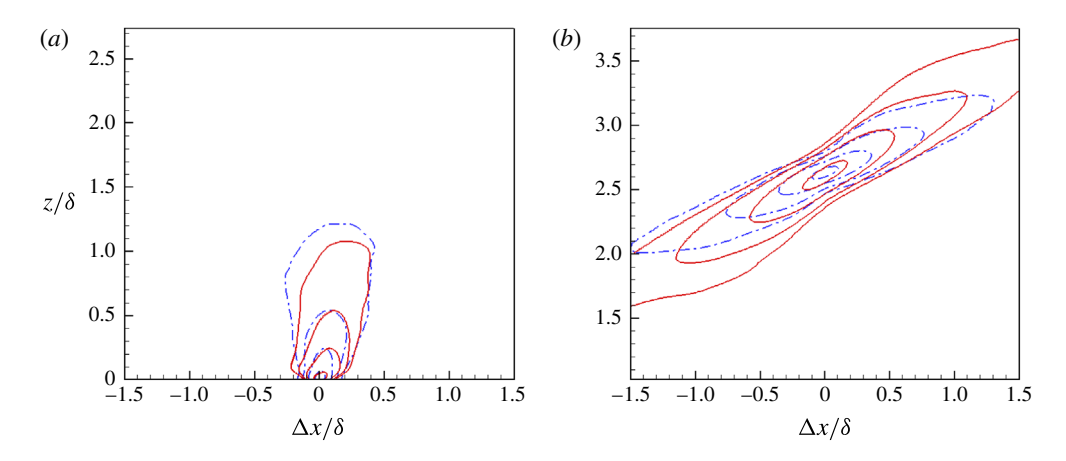


FIGURE 10. (Colour online) Contours of the spatial correlation coefficient of the pressure signal $C_{pp}(\Delta x, 0, 0, x_a, z, z_{ref})$ in the streamwise wall-normal plane: (a) $z_{ref} = 0$ (wall); (b) $z_{ref} = z_{\infty}$ (free stream); —, M6Tw025; — · —, M6Tw076. Four contour levels are shown: $C_{pp} = 0.1$, 0.2, 0.4 and 0.8.

4.4. Propagation and evolution of pressure structures

To quantify the overall propagation speed of pressure-carrying eddies or wavepackets as a function of distance from the wall, the bulk propagation speed is obtained as

$$U_b \equiv -\frac{\overline{(\partial p/\partial t)(\partial p/\partial x)}}{\overline{(\partial p/\partial x)^2}}.$$
(4.3)

This expression defines the bulk propagation speed U_b by finding the value of U_b that minimizes the difference between the real time evolution of p(x, t) and a propagating frozen wave $p(x - U_b t)$. A figure of merit for the frozen-wave approximation can be

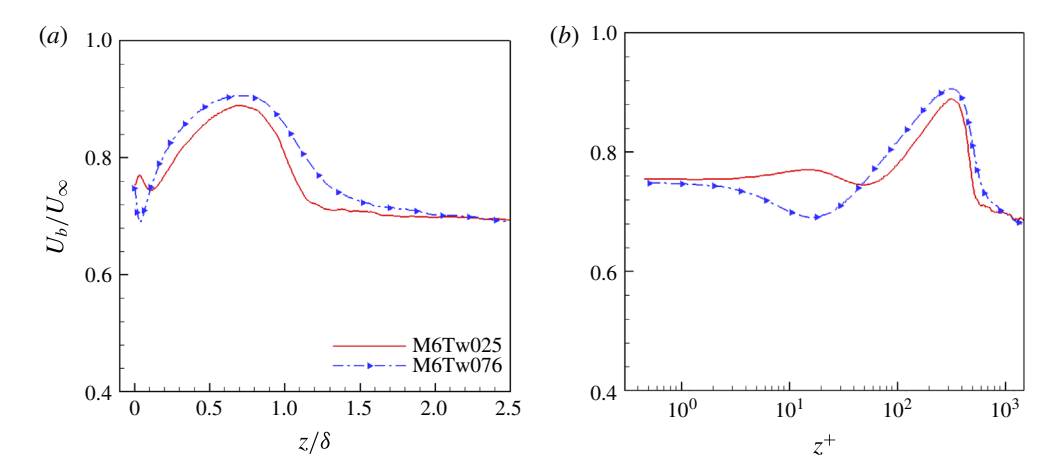


FIGURE 11. (Colour online) Comparison of the bulk propagation speed of pressure fluctuations in (a) outer and (b) inner units between cases M6Tw025 and M6Tw076. Here, U_b is defined based on (4.3).

further defined as

$$\gamma_p \equiv \frac{\left| \overline{(\partial p/\partial x)(\partial p/\partial t)} \right|}{\left[\overline{(\partial p/\partial t)^2} \overline{(\partial p/\partial x)^2} \right]^{1/2}},\tag{4.4}$$

where γ_p equals unity for a perfectly frozen wave and is zero for fast decaying or deforming waves as they convect downstream. This definition of the bulk propagation speed and figure of merit for the frozen-wave approximation was first used by Del Álamo & Jiménez (2009) for the streamwise velocity fluctuations in turbulent channel flows.

Figure 11 shows a comparison of the bulk propagation speed U_b between cases M6Tw025 and M6Tw076. Wall cooling has a small influence on the propagation speed of pressure structures within the main part of the boundary layer and has nearly no influence on the propagation speed of radiated pressure waves in the free stream. Consistent with previous findings (Duan *et al.* 2014, 2016), the free-stream propagation speed for case M6Tw025 is significantly lower than the mean velocity in the free stream.

Figure 12 shows the wall-normal distribution of γ_p which provides a figure of merit for the frozen-wave approximation for cases M6Tw025 and M6Tw076. For both wall-temperature conditions, γ_p is close to unity across the boundary layer, indicating that the propagation effect is overall more dominant than the evolution effect for the pressure structures. As the wall temperature decreases, the pressure structures become more 'frozen', with less significant evolution as they propagate downstream, especially for the pressure structures in the free stream.

The propagation and evolution of large-scale pressure structures can be further investigated via the space-time correlation contours of pressure fluctuations, $C_{pp}(\Delta x, 0, \Delta t, x_a, z_{ref}, z_{ref})$. Figure 13 shows contours of constant space-time correlation $C_{pp}(\Delta x, 0, \Delta t, x_a, z_{ref}, z_{ref})$ at the wall $(z_{ref} = 0)$ and in the free stream $(z_{ref} = z_{\infty})$ for cases M6Tw025 and M6Tw076. The skewed shape of the contours at both locations indicates the propagative nature of the pressure field, which is characterized by downstream propagation of either the coherent pressure-carrying

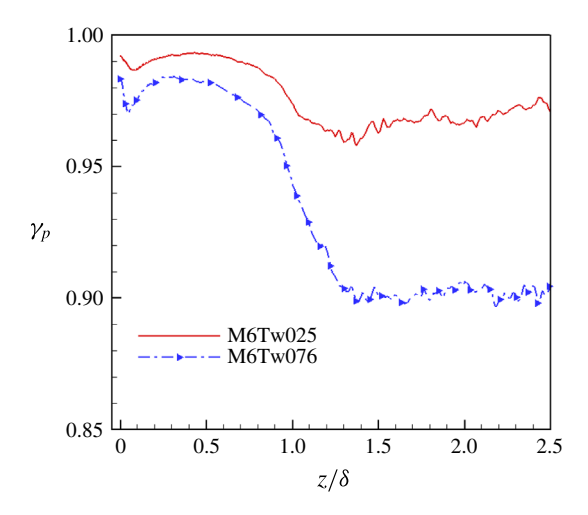


FIGURE 12. (Colour online) The distribution of the correlation coefficient γ_p which provides a figure of merit for the frozen-wave approximation. Here, γ_p is defined based on (4.4).

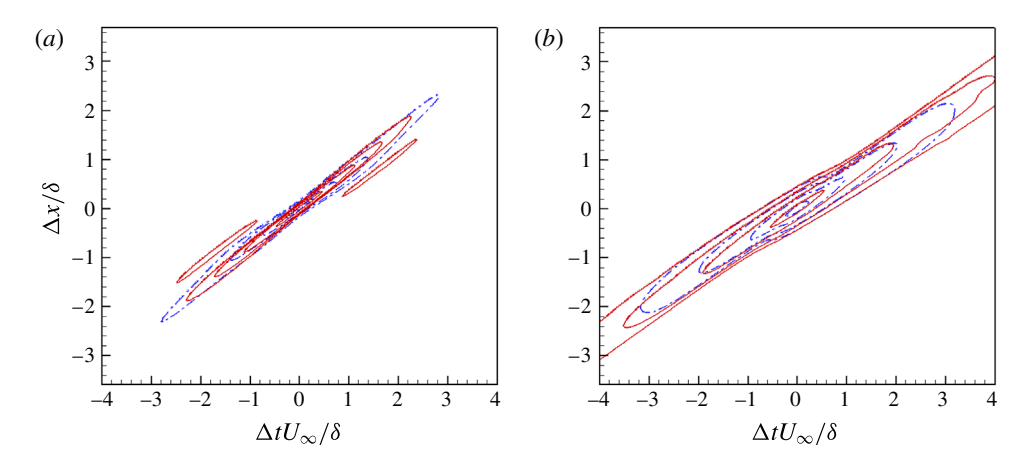


FIGURE 13. (Colour online) Contours of constant space–time correlation coefficient of the pressure signal $C_{pp}(\Delta x, 0, \Delta t, x_a, z_{ref}, z_{ref})$: (a) at the wall; (b) in the free stream; ——, M6Tw025; — · —, M6Tw076. Four contour levels are shown: $C_{pp} = 0.1, 0.2, 0.4$ and 0.8.

eddies within the boundary layer or the pressure wavepackets in the free stream. Based on the space-time correlation data, the speed of propagation of pressure fluctuations can be estimated as the ratio $\Delta x/\Delta t$ for a given time delay Δt at the value of Δx where

$$\frac{\partial C(r_x, 0, \Delta t, x_a, z_{ref}, z_{ref})}{\partial r_x} \bigg|_{r_x = \Delta x} = 0, \tag{4.5}$$

or for a given streamwise separation Δx at the value of Δt where

$$\left. \frac{\partial C(\Delta x, 0, r_t, x_a, z_{ref}, z_{ref})}{\partial r_t} \right|_{r_t = \Delta t} = 0. \tag{4.6}$$

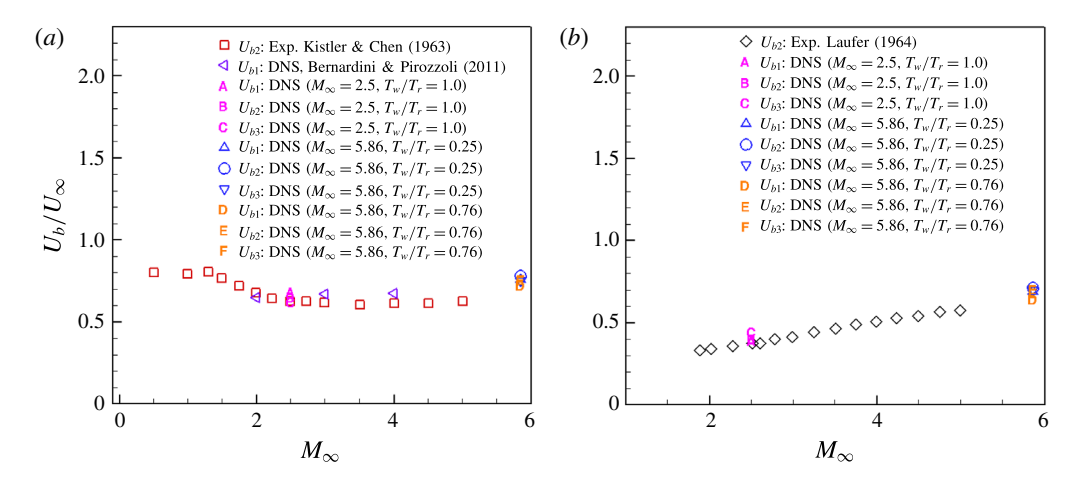


FIGURE 14. (Colour online) Bulk propagation speeds of the pressure fluctuation as a function of free-stream Mach number: (a) at the wall ($z_{ref} = 0$); (b) in the free stream ($z_{ref} = z_{\infty}$). Symbols: squares, Kistler & Chen (1963); left triangles, Bernardini & Pirozzoli (2011); diamonds, Laufer (1964); letters A, B, C, Duan *et al.* (2014); up triangle, circle, down triangle, case M6Tw025; letters D, E, F, case M6Tw076. Here, U_{b1} , U_{b2} and U_{b3} are defined based on (4.5), (4.6) and (4.3) respectively.

Figures 14(a) and 14(b) compare the variation of bulk propagation speed with the free-stream Mach number at the wall and in the free stream respectively with some existing experiments and simulations. In the figure, U_{b1} is defined based on the space-time correlation coefficient, with (4.5) for the time delay Δt or frequency ($\omega = 2\pi/\Delta t$) where the premultiplied frequency spectrum (figures 6 and 7) attains its maximum. In analogy, U_{b2} is derived based on (4.6) for the streamwise separation Δx or wavenumber ($k_1 = 2\pi/\Delta x$) where the premultiplied one-dimensional wavenumber spectrum attains its maximum. The value of U_{b3} is computed using (4.3) by assuming a 'frozen wave/eddy'. Consistent with figure 11, the propagation speed based on the space-time correlation coefficient is comparable between cases M6Tw025 and M6Tw076, indicating that wall cooling has only a small influence on the overall propagation speed of pressure structures away from the wall. The Mach-number dependence of the bulk propagation speed is consistent with the previous data reported by Bernardini & Pirozzoli (2011) for U_b at the wall and by Laufer (1964) and Duan *et al.* (2014, 2016) for U_b in the free stream.

To study the propagation speed of spectral components of pressure fluctuations, the phase speed of pressure fluctuations is defined as

$$U_p(\omega) = \omega \Delta x / \theta_p(\omega), \tag{4.7}$$

where Δx is the distance between two pressure signals separated in the streamwise direction and $\theta_p(\omega)$ is the phase difference between the two streamwise-separated pressure signals derived based on the cross-spectrum of the two signals. In the current study, the streamwise separation Δx is chosen to be the smallest streamwise distance at which two pressure signals are spatially sampled ($\Delta x^+ = 6.42$ and 28.9 for cases M6Tw025 and M6Tw076 respectively). At the selected streamwise separation, the coherence between the two signals is close to unity and the definition (4.7) thus provides a 'local' measurement of the phase speed. This definition was first used by

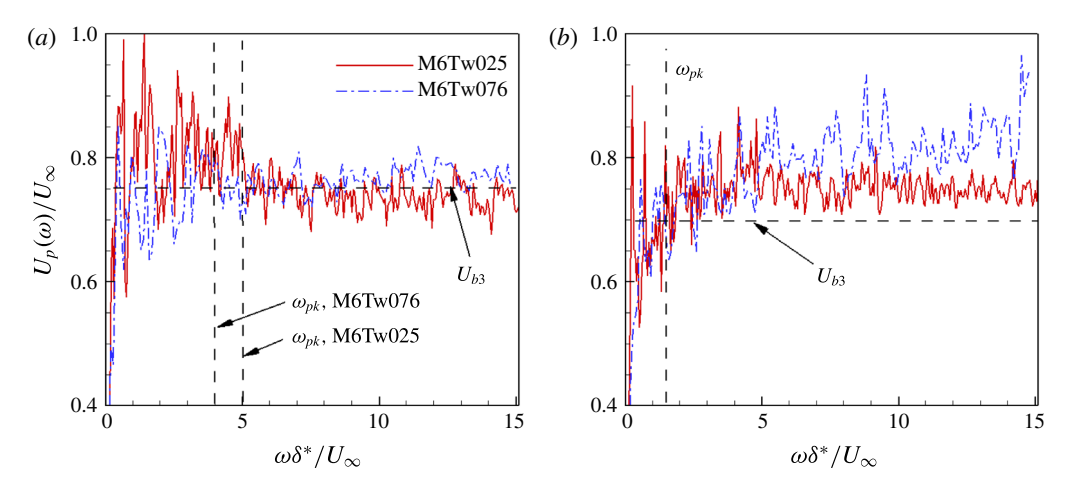


FIGURE 15. (Colour online) Comparison of phase speed (a) at the wall and (b) in the free stream. The phase speed $U_p(\omega)$ is defined based on equation (4.7). The vertical dashed line denotes the peak frequency ω_{pk} where the premultiplied frequency spectrum attains its maximum.

Stegen & Van Atta (1970) to measure the local phase speed of the Fourier components of the longitudinal velocity fluctuations in grid turbulence with a small probe spacing. Figure 15 shows the phase speed of pressure fluctuations $U_p(\omega)$ at the wall and in the free stream. At the wall, the phase speed shows a weak frequency dependence for both cases, and the wall-pressure structures of all frequencies propagate with speeds similar to the local bulk propagation speed. In the free stream, while the phase speed of the dominant pressure structures is similar to the local bulk propagation speed, wall cooling slightly increases the free-stream phase speed at higher frequencies, and the high-frequency pressure structures propagate with a speed larger than the bulk propagation speed.

To interpret the Lagrangian decorrelation length of the coherent pressure structures, Figure 16 compares the spatial decay of the maximum space–time correlation of pressure fluctuations, $(C_{pp})_{max}$, at the wall and in the free stream for cases M6Tw025 and M6Tw076. The slower rate of spatial decay in $(C_{pp})_{max}$ for case M6Tw025 indicates that wall cooling de-energizes pressure structures, making them evolve less rapidly as they propagate downstream. Such a trend is consistent with the larger values of the 'frozen-wave' index γ_p (figure 12) for case M6Tw025.

4.5. Free-stream acoustic radiation

In this section, the nature of free-stream acoustic fluctuations radiated from the turbulent boundary layer is analysed, including the modal compositions and the acoustic sources.

4.5.1. Modal compositions of free-stream fluctuations

The characteristics of free-stream fluctuations are analysed using the theory of modal analysis, which was initially proposed by Kovasznay (1953). According to Kovasznay, the fluctuations at any point within a uniform mean flow can be represented as a superposition of three different modes with covarying physical properties: the vorticity mode, the acoustic or sound-wave mode and the entropy mode (also referred to as entropy spottiness or temperature spottiness).

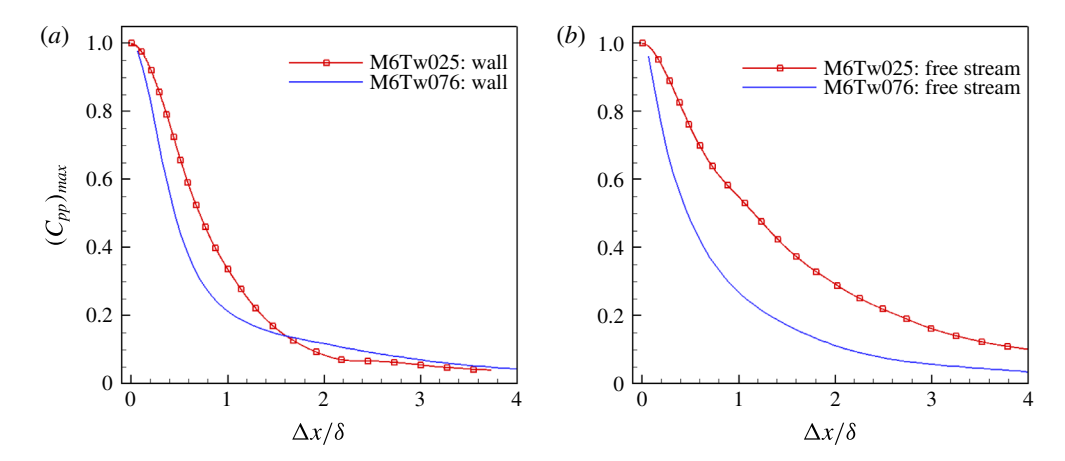


FIGURE 16. (Colour online) Comparison of the maximum space—time correlation coefficient of pressure fluctuations, $(C_{pp})_{max}$, as a function of streamwise separation Δx (a) at the wall and (b) in the free stream for cases M6Tw025 and M6Tw076.

	M6Tw076	M6Tw025
u'_{rms}/\overline{u}	1.36×10^{-3}	2.34×10^{-3}
v'_{rms}/\overline{u}	1.05×10^{-3}	1.62×10^{-3}
w'_{rms}/\overline{u}	2.05×10^{-3}	3.20×10^{-3}
p'_{rms}/\overline{p}	2.05×10^{-2}	3.47×10^{-2}
$ ho_{rms}^{\prime}/\overline{ ho}$	1.46×10^{-2}	2.48×10^{-2}
T'_{rms}/\overline{T}	5.89×10^{-3}	9.89×10^{-3}
$(\rho u)'_{rms}/\overline{\rho u}$	1.38×10^{-2}	2.29×10^{-2}
$T'_{t,rms}/\overline{T}_t$	1.98×10^{-3}	3.08×10^{-3}
$p'_{t,rms}/\overline{p}_t$	6.69×10^{-3}	1.08×10^{-2}
$\overline{(\partial u_i'/\partial x_i)^2}/\overline{\Omega_i'\Omega_i'}$	31 580	12 153
s'_{rms}/R	2.11×10^{-3}	2.29×10^{-4}
$\overline{u'p'}/u'_{rms}p'_{rms}$	-0.653	-0.829
$\overline{v'p'}/v'_{rms}p'_{rms}$	-0.00639	-0.00512
$\overline{w'p'}/w'_{rms}p'_{rms}$	0.925	0.956
$\overline{\rho'p'}/\rho'_{rms}p'_{rms}$	1	1
$\overline{T'p'}/T'_{rms}p'_{rms}$	1	1

TABLE 4. The free-stream disturbance field for cases M6Tw025 and M6Tw076. Here, R is the gas constant in the ideal-gas equation of state $p = \rho RT$.

Table 4 lists the free-stream values of several fluctuating flow variables for cases M6Tw025 and M6Tw076. Here, s is the specific entropy, Ω is the vorticity and the subscript 't' denotes stagnation quantities. A comparison of the data in the two cases indicates that the magnitude of free-stream fluctuations normalized by the respective mean values increases significantly as the wall temperature decreases, including both the velocity fluctuations and the fluctuations in thermodynamic variables. In particular, the pressure fluctuations in the free stream, including p'_{rms}/\bar{p} and $p'_{t,rms}/\bar{p}_t$, are considerably different for the two cases (3.47% versus 2.05% for p'_{rms}/\bar{p} , 1.08%

versus 0.669% for $p'_{t,rms}/\bar{p}_t$, larger values for the colder-wall case). However, p'_{rms}/\bar{p}_t and $p'_{t,rms}/\bar{p}_t$ bear nearly the same ratio of approximately 1.7 across the two cases. For both wall-temperature cases, the variation in r.m.s. amplitudes of velocity fluctuations along the three Cartesian axes indicates the anisotropy of the free-stream velocity fluctuations, with the wall-normal component of the velocity fluctuations being the largest among the three. The relative perturbations in thermodynamic variables are nearly an order of magnitude larger than the velocity fluctuations and nearly satisfy isentropic relations, indicating the acoustic nature of the free-stream fluctuations. The dominance of the acoustic model is also indicated by the large ratio of the dilatational fluctuations $(\partial u'_i/\partial x_i)^2$ to the vortical fluctuations Ω'_i/Ω'_j and the small values of the entropy fluctuations s'_{rms}/R compared with the pressure fluctuations p'_{rms}/\bar{p} .

Laufer (1964) had assumed the u' and p' fluctuations to be perfectly anticorrelated during the reduction of his hot-wire measurements based on the assumption of purely planar acoustic waves. However, the numerical simulations for both values of surface temperature ratio show that the correlation coefficient between u' and p' is different from -1. Cooling of the surface leads to a correlation coefficient of -0.829 for case M6Tw025, which is closer to -1 than the correlation coefficient of -0.653 for case M6Tw076. The less significant deviation from purely planar behaviour for case M6Tw025 may indicate that acoustic radiation becomes closer to planar acoustic waves with increased wall cooling.

4.5.2. Acoustic sources

To understand the effect of wall cooling on the pressure field, an analysis following Phillips (1960) has been carried out to study the acoustic sources that are responsible for the pressure fluctuations induced by the turbulent boundary layer. The acoustic source terms can be derived by rearranging the Navier–Stokes equations into the form of a wave equation, after neglecting the diffusive terms, as

$$\left\{ \frac{D^2}{Dt^2} - \frac{\partial}{\partial x_i} a^2 \frac{\partial}{\partial x_i} \right\} \log \left(\frac{p}{p_0} \right) = \gamma S, \tag{4.8}$$

where $S = (\partial u_i/\partial x_j)(\partial u_j/\partial x_i)$ is the acoustic source term, which is quadratic in the total flow velocity, p_0 is a convenient reference pressure, D/Dt is the substantial derivative based on mean flow velocity and γ is the specific heat ratio. The terms on the left-hand side of (4.8) are those of a wave equation in a medium moving with the local mean velocity of the flow. The acoustic source term S on the right-hand side can be further decomposed into its linear (rapid) component $2(\partial \bar{U}/\partial z)(\partial w'/\partial x)$ and its nonlinear (slow) component $(\partial u_i'/\partial x_j)(\partial u_j'/\partial x_i)$. The details about the acoustic analogy equation, the definition and the decomposition of acoustic source terms are discussed in our previous papers (Duan $et\ al.\ 2014,\ 2016$).

Figure 17 plots the r.m.s. of the acoustic source term, S'_{rms} , and its linear and nonlinear components in the near-wall region of the boundary layer against wall-normal distance. For both wall temperatures, the near-wall variation of the total acoustic source term conforms well with that of p'_{rms} (figure 5b). For case M6Tw076, the nonlinear source term is dominant over the linear term throughout the boundary layer (figure 17a), and $(\partial v'/\partial z)(\partial w'/\partial y)$ has the largest r.m.s. value among the constituent terms of the nonlinear acoustic source (figure 17c). The dominance of $(\partial v'/\partial z)(\partial w'/\partial y)$ may be indicative of the important role played by streamwise vortical structures in sound generation (Duan et al. 2016).

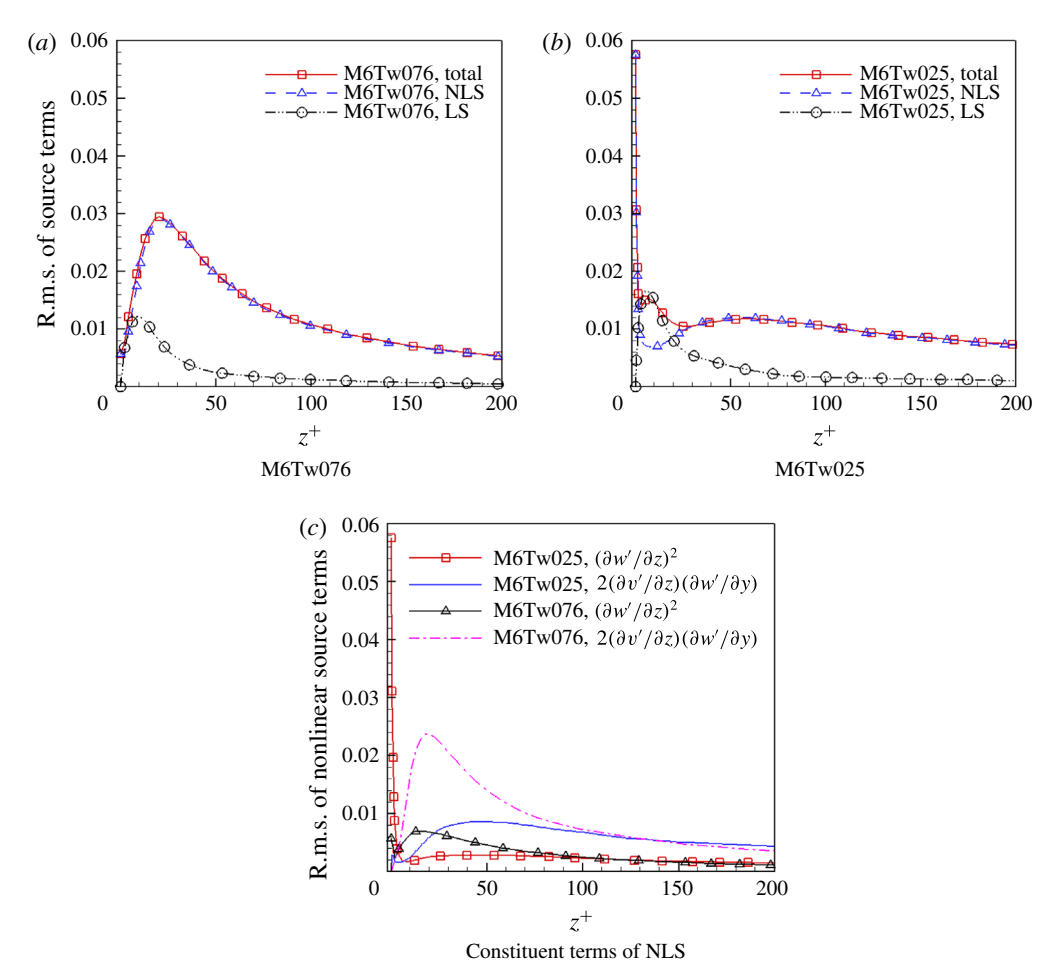


FIGURE 17. (Colour online) Profiles of the r.m.s. source terms (including the total, nonlinear source (NLS) and linear source (LS) terms) across the near-wall portion of the boundary layer. The r.m.s. values of the source terms are normalized by $(\nu_w/u_\pi^2)^2$.

As the wall temperature is decreased, the r.m.s. of the nonlinear acoustic term is significantly reduced in the buffer layer due to the damping of $(\partial v'/\partial z)(\partial w'/\partial y)$, and the linear source term becomes relatively more dominant in this region (figure 17b). In the meantime, the r.m.s. value of the nonlinear acoustic term is dramatically increased in the viscous sublayer, with $(\partial w'/\partial z)^2$ becoming the most dominant term in this region (figure 17c). Given that $(\partial w'/\partial z)^2$ is related to the dilatational fluctuations of velocity and $(\partial v'/\partial z)(\partial w'/\partial y)$ is related to the near-wall streamwise vortical fluctuations, the variation of these terms with wall temperature may indicate that wall cooling influences sound generation largely by enhancing dilatational motions in the viscous sublayer while damping streamwise vortical structures in the buffer layer. The enhancement of the dilatational motions in the viscous sublayer and the damping of the streamwise vortical structures in the boundary layer are also apparent from the rapid increase in r.m.s. dilation and r.m.s. streamwise vorticity near the wall, as seen from figures 18(a) and 18(b). The enhancement of dilatational motions near the wall is not unexpected as wall cooling increases the turbulent Mach number by causing a decrease in the local sound speed.

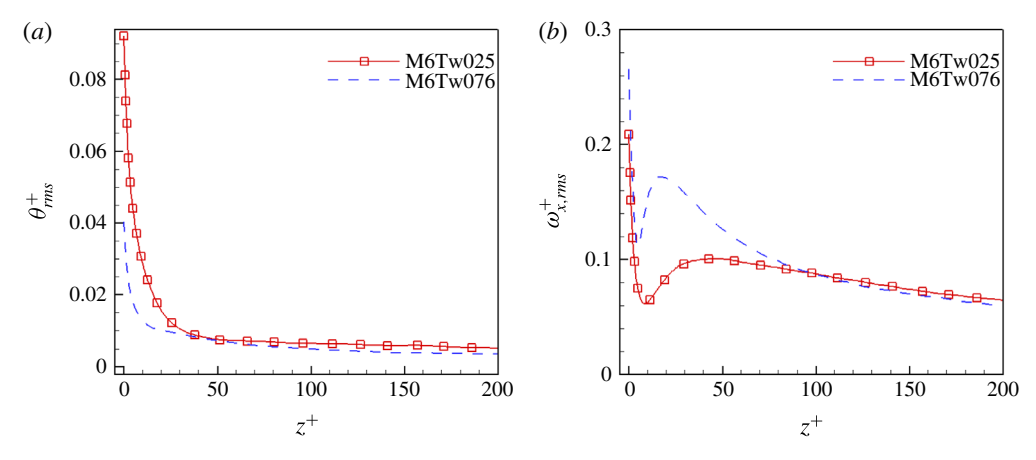


FIGURE 18. (Colour online) Profiles of the r.m.s. of dilatation and streamwise vorticity across the near-wall portion of the boundary layer normalized using v_w/u_τ^2 .

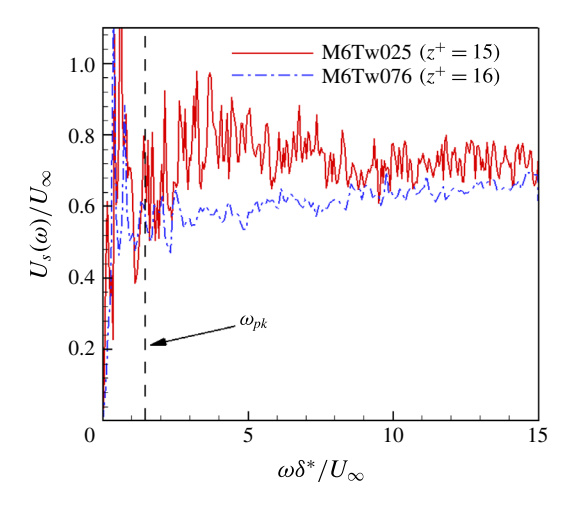


FIGURE 19. (Colour online) The phase speed of the acoustic source term. Here, $U_s(\omega)$ is defined based on (4.7) for the acoustic source term S.

Figure 19 compares the phase speed derived from the acoustic source term, $U_s(\omega)$, between cases M6Tw025 and M6Tw076 in the buffer layer. Wall cooling increases the convection speed of the acoustic sources for all frequencies. At the dominant frequency of free-stream acoustic radiation, $\omega_{pk}\delta/U_{\infty}=1.5$, which corresponds to the peak frequency of the premultiplied spectrum shown in figure 7(c), the convection speed of the acoustic source is $0.64U_{\infty}$ ($M_r=2.11$) and $0.55U_{\infty}$ ($M_r=2.64$) respectively for cases M6Tw025 and M6Tw076, with $M_r\equiv (U_{\infty}-U_s)/a_{\infty}$. The fact that acoustic sources propagate supersonically with respect to the free stream is consistent with the concept of 'eddy Mach wave' radiation (Phillips 1960). Given that the radiation wave angle can be approximated via the 'Mach angle' relation as $1/\sin\theta=M_r$, the smaller value of M_r for case M6Tw025 is consistent with the larger radiation wave angle of 28° for this case (figure 10b).

5. Summary and conclusions

Direct numerical simulations of Mach 5.86 turbulent boundary layers with two wall temperatures $(T_w/T_r = 0.25, 0.76)$ are compared to investigate the effect of wall cooling on the pressure fluctuations generated by hypersonic turbulent boundary layers. The simulations show that wall cooling significantly modifies the pressure-fluctuation intensities near the wall, with $p'_{w rms}/\tau_w$ varying from 2.8 for $T_w/T_r = 0.76$ to 3.5 for $T_w/T_r = 0.25$. Furthermore, the frequency spectra of the wall-pressure fluctuations for the two cases show considerable differences when plotted in terms of either outer-layer or inner-layer variables. The peak of the premultiplied spectrum shifts to a higher value as the wall temperature decreases. Wall cooling slows down the evolution of pressure wavepackets at the wall, resulting in a larger decorrelation length of pressure structures, but has little influence on the bulk propagation speeds of wall-pressure structures. Regarding the free-stream pressure fluctuations, although the intensity shows a strong wall-temperature dependence when normalized by the mean free-stream pressure (\bar{p}_{∞}) , it compares well between the two cases when normalized by the local wall shear stress τ_w . The frequency spectra of free-stream radiation collapse well between the two cases when normalized in terms of outer or inner boundary-layer parameters. Wall cooling results in an increase in the radiation wave angle (defined based on spatial correlations, C_{pp}) from 21° for $T_w/T_r = 0.76$ to 28° for $T_w/T_r = 0.25$. Similarly to pressure structures at the wall, the free-stream pressure structures evolve less rapidly as the wall temperature decreases. The propagation speed of free-stream pressure structures is found to be insensitive to the wall temperature and is significantly smaller than the free-stream velocity for both cases. An analysis of acoustic sources using the acoustic analogy of Phillips (1960) shows that wall cooling influences sound generation largely by enhancing dilatational motions in the viscous sublayer while damping streamwise vortical structures in the buffer layer.

Acknowledgements

This material is based on work supported by the Air Force Office of Scientific Research through award no. FA9550-14-1-0170, managed by Dr I. Leyva. The work was initiated with support of the NASA Langley Research Center under the Research Cooperative agreement no. NNL09AA00A (through the National Institute of Aerospace). Computational resources were provided by the NASA Advanced Supercomputing Division, the DoD High Performance Computing Modernization Program and the NSF's PRAC program (NSF ACI-1640865).

REFERENCES

BERESH, S. J., HENFLING, J. F., SPILLERS, R. W. & PRUETT, B. O. M. 2011 Fluctuating wall pressures measured beneath a supersonic turbulent boundary layer. *Phys. Fluids* 23 (7), 075110.

BERNARDINI, M. & PIROZZOLI, S. 2011 Wall pressure fluctuations beneath supersonic turbulent boundary layers. *Phys. Fluids* **23** (8), 085102.

BERNARDINI, M., PIROZZOLI, S. & GRASSO, F. 2011 The wall pressure signature of transonic shock/boundary layer interaction. *J. Fluid Mech.* 671, 288–312.

BLAKE, W. K. 1986 Mechanics of Flow-Induced Sound and Vibration. Academic Press.

BOWERSOX, R. D. W. 2009 Extension of equilibrium turbulent heat flux models to high-speed shear flows. *J. Fluid Mech.* **633**, 61–70.

BULL, M. K. 1996 Wall-pressure fluctuations beneath turbulent boundary layers: some reflection on forty years of research. *J. Sound Vib.* **190** (3), 299–315.

- CHU, Y. B., ZHANG, Y. Q. & LU, X. Y. 2013 Effect of wall temperature on hypersonic turbulent boundary layer. *J. Turbul.* **14** (12), 37–57.
- DEL ÁLAMO, J. C. & JIMÉNEZ, J. 2009 Estimation of turbulent convection velocities and corrections to Taylor's approximation. *J. Fluid Mech.* **640**, 5–26.
- DI MARCO, A., CAMUSSI, R., BERNARDINI, M. & PIROZZOLI, S. 2013 Wall pressure coherence in supersonic turbulent boundary layers. *J. Fluid Mech.* **732**, 445–456.
- DUAN, L., BEEKMAN, I. & MARTÍN, M. P. 2010 Direct numerical simulation of hypersonic turbulent boundary layers. Part 2: effect of wall temperature. *J. Fluid Mech.* 655, 419–445.
- DUAN, L., CHOUDHARI, M. M. & WU, M. 2014 Numerical study of pressure fluctuations due to a supersonic turbulent boundary layer. *J. Fluid Mech.* **746**, 165–192.
- DUAN, L., CHOUDHARI, M. M. & ZHANG, C. 2016 Pressure fluctuations induced by a hypersonic turbulent boundary layer. *J. Fluid Mech.* **804**, 578–607.
- FERNHOLZ, H. H., DUSSAUGE, J. P., FINLAY, P. J., SMITS, A. J. & RESHOTKO, E. 1989 A survey of measurements and measuring techniques in rapidly distorted compressible turbulent boundary layers. *AGARDograph* **315**, 1–18.
- FERNHOLZ, H. H. & FINLEY, P. J. 1980 A critical commentary on mean flow data for two-dimensional compressible turbulent boundary layers. *AGARDograph* **253**, 1–221.
- HADJADJ, A., BEN-NASR, O., SHADLOO, M. S. & CHAUDHURI, A. 2015 Effect of wall temperature in supersonic turbulent boundary layers: a numerical study. *Intl J. Heat Mass Transfer* 81, 426–438.
- HUANG, P. G., COLEMAN, G. N. & BRADSHAW, P. 1995 Compressible turbulent channel flows: DNS results and modelling. *J. Fluid Mech.* **305**, 185–218.
- KISTLER, A. L. & CHEN, W. S. 1963 The fluctuating pressure field in a supersonic turbulent boundary layer. *J. Fluid Mech.* **16**, 41–64.
- KOVASZNAY, L. S. G. 1953 Turbulence in supersonic flow. J. Aero. Sci. 20, 657-674.
- LAGHA, M., KIM, J., ELDREDGE, J. D. & ZHONG, X. 2011 A numerical study of compressible turbulent boundary layers. *Phys. Fluids* 23 (1), 015106.
- LAUFER, J. 1964 Some statistical properties of the pressure field radiated by a turbulent boundary layer. *Phys. Fluids* **7** (8), 1191–1197.
- LELE, S. K. 1994 Compressibility effects on turbulence. Annu. Rev. Fluid Mech. 26, 211-254.
- MAEDER, T. 2000 Numerical investigation of supersonic turbulent boundary layers. PhD thesis, ETH, Zürich.
- MODESTI, D. & PIROZZOLI, S. 2016 Reynolds and Mach number effects in compressible turbulent channel flow. *Intl J. Heat Fluid Flow* **59**, 33–49.
- MORKOVIN, M. V. 1962 Effects of compressibility on turbulent flows. In *Mécanique de la Turbulence* (ed. A. J. Favre), pp. 367–380. CNRS.
- PELTIER, S. J., HUMBLE, R. A. & BOWERSOX, R. D. W. 2016 Crosshatch roughness distortions on a hypersonic turbulent boundary layer. *Phys. Fluids* 28 (4), 045105.
- PHILLIPS, O. M. 1960 On the generation of sound by supersonic turbulent shear layers. *J. Fluid Mech.* 9, 1–28.
- POGGIE, J. 2015 Compressible turbulent boundary layer simulations: resolution effects and turbulence modeling. *AIAA Paper* 2015-1983.
- SCHLATTER, P. & ÖRLÜ, R. 2010 Assessment of direct numerical simulation data of turbulent boundary layers. *J. Fluid Mech.* **659**, 116–126.
- SCHNEIDER, S. P. 2001 Effects of high-speed tunnel noise on laminar-turbulent transition. *J. Spacecr. Rockets* 38 (3), 323–333.
- SHADLOO, M. S., HADJADJ, A. & HUSSAIN, F. 2015 Statistical behavior of supersonic turbulent boundary layers with heat transfer at $M_{\infty} = 2$. Intl J. Heat Fluid Flow 53, 113–134.
- SHAHAB, M. F., LEHNASCH, G., GATSKIEMAIL, T. B. & COMTE, P. 2011 Statistical characteristics of an isothermal, supersonic developing boundary layer flow from DNS data. *Flow Turbul. Combust.* **86** (3), 369–397.
- SMITS, A. J. 1991 Turbulent boundary layer structure in supersonic flow. *Phil. Trans. R. Soc. Lond.* A **336** (1), 81–93.

- SMITS, A. J. & DUSSAUGE, J. P. 2006 Turbulent Shear Layers in Supersonic Flow, 2nd edn. American Institute of Physics.
- STEEN, L. E. 2010 Characterization and development of nozzles for a hypersonic quiet wind tunnel. Master's thesis, Purdue University, West Lafayette, IN, USA.
- STEGEN, G. R. & VAN ATTA, C. W. 1970 A technique for phase speed measurements in turbulent flows. J. Fluid Mech. 42, 689-699.
- TRETTEL, A. & LARSSON, J. 2016 Mean velocity scaling for compressible wall turbulence with heat transfer. *Phys. Fluids* **28** (2), 026102.
- TSUJI, Y., FRANSSON, J. H. M., ALFERDSSON, P. H. & JOHANSSON, A. V. 2007 Pressure statistics and their scaling in high-Reynolds-number turbulent boundary layers. *J. Fluid Mech.* **585**, 1–40.
- WALZ, A. 1969 Boundary Layers of Flow and Temperature. MIT Press.
- WELCH, P. D. 1967 The use of fast Fourier transform for the estimation of power spectra: a method based on time averaging over short, modified periodograms. *IEEE Trans. Audio Electroacoust.* AU-15, 70–73.
- Wu, B., BI, W., Hussain, F. & She, Z.-S. 2017 On the invariant mean velocity profile for compressible turbulent boundary layers. *J. Turbul.* **18**, 186–202.
- ZHANG, Y., BI, W., HUSSAIN, F. & SHE, Z. 2014 A generalized Reynolds analogy for compressible wall-bounded turbulent flows. *J. Fluid Mech.* **739**, 392–420.